Thermally-Induced Morphological Evolution of Spherical Silica Nanoparticles using *in-operando* X-ray Scattering Measurements

Hassnain Asgar,[1] Viktoriya Semeykina,[2] Mikaila Hunt,[2] Sohaib Mohammed,[1] Ivan Kuzmenko,[3] Ilya Zharov,[2] and Greeshma Gadikota[1,*]

[1]School of Civil and Environmental Engineering, Cornell University, Ithaca, NY 14850

[2]Department of Chemistry, University of Utah, Salt Lake City, Utah, 84112

[3]X-Ray Science Division, Advanced Photon Source, Building 433A, Argonne National Laboratory, 9700 Cass Avenue, Lemont, IL 60439

Abstract

The assembly and morphology of pores determine thermodynamic, flow and reactive properties of confined fluids. However, there is a limited understanding of how pore architectures dynamically develop in engineered and natural materials. To develop a calibrated understanding of fluid properties in confinement, the synthesis of architected materials has been proposed. The design of geo-architected materials has to be informed by the dynamic evolution of the morphology in response to thermal or chemical events. In this study, we probe thermally induced morphological evolution of spherical silica nanoparticles 220 ± 30 nm in diameter using *in-operando* Ultra-Small and Small Angle X-Ray Scattering measurements. The calcination experiments demonstrated that at temperatures up to 600 °C the pore radii remained in the range of 2.15 nm – 2.35 nm and the particle diameters in the range of 220 ± 30 nm. Sintering these calcined silica nanoparticles to temperatures up to 1050 °C reduced the pore size from 2.2 ± 0.1 nm to ~1.8 – 0.2 nm. These changes corresponded to the formation of siloxane (Si-O-Si) bridges resulting from dehydroxylation. The characteristic pore radius of sintered particles was also confirmed by N_2 adsorption measurements. These studies represent the use of non-invasive dynamic characterization methods such as X-ray scattering to elucidate thermally induced morphological evolution in architected siliceous materials.

Keywords: SiO_2 nanoparticles, sintering, X-ray scattering

1. Introduction

Our known understanding of the properties of thermodynamics ([1–8]), transport ([8–14]), and reactivity ([8,15–17]) of bulk fluids differs significantly from that of confined fluids. These fundamental differences in fluid properties in bulk and confined environments can be harnessed to design novel pathways for separations ([18–22]), and the targeted recovery ([23,24]) or storage of fluids ([25–27]) in natural and engineered environments. To advance a calibrated understanding of these differences, developing design controls on pore architectures is essential. Specifically, our ability to harness and in some cases, transform the morphology of siliceous and carbonaceous materials has yielded several advancements in subsurface and engineered processes. Specific examples include harnessing silica-rich rocks such as sandstone for carbon storage ([28–35]), recovery of hydrocarbons from carbonate-bearing rocks ([36–38]), developing novel carbon ([39–42]) or silica-based materials ([43–46]) for gas separations and conversions, and advancing the next generation of electronic materials and electrochemical systems ([47–51]).

Another challenge that needs to be overcome in the targeted design of porous materials is to develop an alternative approach to the repeated and iterative synthesis of materials till the target morphology and chemistry is achieved. Instead, *in-operando* analyses of the chemical and morphological features allow us to identify the underlying phenomena and design scientifically informed pathways to tune the morphologies and chemistries of porous materials. This research vision has guided the use of non-invasive *in-operando* characterization approaches to elucidate the development of pore structures in architected siliceous materials. In this study, Stöber silica synthesized through ammonia-catalyzed sol-gel process ([52–57]) is one of the material systems of interest for determining fluid properties in confinement. Extensive research efforts have enabled tunable controls on the morphologies of silica nanoparticles by changing the aqueous chemistry

([58–66]) and by heating ([67,68]). Briefly, reactions 1-4 are involved in the synthesis of monodisperse silica nanoparticles using the Stöber process with tetraethoxysilicate (TEOS) as silica precursor ([69–73]). The synthesis reaction begins with the hydrolysis of ethoxy group to form $Si(OC_2H_5)_{4-x}(OH)_x$ intermediate species, where the hydroxyl group substitutes the ethoxy groups in TEOS as given in reaction (1). The ammonia present in the solution acts as a basic catalyst and provides the hydroxyl anions to initiate the reaction. The hydrolysis reaction is followed by the condensation reaction. The condensation reaction could follow the two schemes. The reaction of hydroxyl groups in $Si(OC_2H_5)_{4-x}(OH)_x$ intermediate with either the ethoxy groups of other TEOS, called alcohol condensation, or hydroxyl group of another hydrolysis intermediate, known as water condensation, to form Si-O-Si bridges. Both condensation reactions are presented in reactions (2) and (3), respectively. The overall reaction explaining the synthesis of silica nanoparticles from Stöber process is shown in reaction (4).

$$Si(OC_2H_5)_4 + xH_2O \rightarrow Si(OC_2H_5)_{4-x}(OH)_x + xC_2H_5OH \quad (1)$$

$$\equiv Si\text{-}OC_2H_5 + HO\text{-}Si\equiv \rightarrow \equiv Si\text{-}O\text{-}Si\equiv + C_2H_5OH \quad (2)$$

$$\equiv Si\text{-}OH + HO\text{-}Si\equiv \rightarrow \equiv Si\text{-}O\text{-}Si\equiv + H_2O \quad (3)$$

The overall reaction is:

$$Si(OC_2H_5)_4 + 2H_2O \rightarrow SiO_2 + 4C_2H_5OH \quad (4)$$

While there is extensive understanding of how the solid silica nanoparticles are formed starting from colloidal systems ([56–66,74–77]), there is a limited understanding of how the microstructures of silica nanoparticles evolve during the calcination and sintering of these materials. Understanding these behaviors will allow us to utilize these silica nanoparticles as building blocks to construct geo-architected materials with repeatable heterogeneity to represent naturally occurring materials. Sintering is one of the steps involved in designing geo-architected materials ([78,79]). To deconstruct the dynamic morphological changes as they occur in these materials, the following research questions need to be addressed: (1) How do the pore sizes dynamically change during the calcination and sintering of silica nanoparticles prepared using the Stöber process? (2) What are the corresponding chemical changes associated with the evolving morphological features?

To elucidate thermally induced morphological changes that occur in these materials, we harness *in-operando* synchrotron based Ultra-Small Angle X-ray Scattering (USAXS) and Small Angle X-Ray Scattering (SAXS) techniques in combination (described as USAXS/SAXS) ([80–82]). This approach allows us to map the morphological features from sub-nanometer range to a few microns (~6 μm) ([83,84]). The changes in the pore size distribution and surface area were also measured using N_2 adsorption. The relatively fast scans to the order of three to five minutes allow us to capture the *in-operando* changes in the morphological features. The chemical changes as a result of the thermal treatment are determined using Attenuated Total Reflection-Fourier Transform Infrared Spectroscopy (ATR-FTIR). In this study, we evaluate the hypothesis that sintering of silica nanoparticles yields smaller and compact pores. The experimental approach and the results are discussed in the following sections.

2. Materials and Methods

2.1 Synthesis of SiO_2 nanoparticles

Monodisperse silica particles with a diameter of 220 ± 30 nm were prepared by the modified Stöber method. Briefly, 11 ml of tetraethoxysilicate (TEOS, Alfa Aesar, 99+ %) was added to 114 ml of absolute ethanol (Decon Labs) under rigorous stirring at room temperature (~20 °C) in a 500 ml flat-bottomed flask. In a separate flask, a mixture of 7 ml of ammonia (VWR

Chemical, 28 wt.% aqueous solution, ACS grade), 72 ml of deionized water, and 46 ml of ethanol was prepared. The latter solution was added to the former mixture rapidly and stirring constantly for 24 hours. Silica nanoparticles were separated from the solution via centrifugation at the acceleration force of 5000×g. Finally, the nanoparticles were washed with deionized water until neutral pH was reached. The silica nanoparticles were dried in a vacuum oven for 24 hours at room temperature.

2.2 Experimental Setup and Characterization

The *in-operando* USAXS/SAXS measurements were performed to determine the morphological changes during the thermal treatment of silica nanoparticles. The measurements were performed at Sector 9-ID at Advanced Photon Source (APS) in Argonne National Laboratory (ANL), Argonne, IL using the original Bonse-Hart double-crystal setup [85,86]. During the measurements, the total X-ray flux, energy, and wavelength at the sample position were ~10^{13} photon cm^{-2} s^{-1}, 21.0 keV, and 0.59 Å, respectively. Instrument calibrations were performed using silver behenate[87]. Nika [88] and Irena [89] macros embedded in the IgorPro software (Wavemetrics, Lake Oswego, OR) were used for data reduction and analysis. The *in-operando* measurements were performed in the Linkam TS1500 heating stage (Linkam Scientific Instruments Ltd., Tadworth, UK) and completed in two steps. In the first step, the pelletized sample was heated up to the calcination temperature (600 °C) with a temperature ramp of 5 °C/min and then isothermally heated for 4 hours. In the second step, following the calcination, the sample was cooled down to 35 °C and then reheated to 1050 °C with a ramp of 5 °C/min following the isothermal sintering at 1050 °C.

To capture the hierarchical morphological features in these materials, the USAXS/SAXS data were modeled using the "Modeling II" tool in Irena package [89]. For this purpose, three levels of fittings were performed in three different q regions, where $q = (4\pi/\lambda)\sin(\theta/2)$ and λ is the wavelength of incident X-ray and θ is the scattering angle [90]. In the low q-region (<0.002 Å^{-1}), which represents the scattering response of larger microstructural features to the order of several hundred nanometers or a few micrometers, unified fit model was employed. This model is based on the approach proposed by Beaucage ([91,92]). The fit in each level can be described by a Guinier regime and a power-law regime. Although the model assumes spherical and centrosymmetric shape of particles [92], it can be applied to a range of scatterer shapes, like spheres, rods, lamellae, and cylinders, based on its formulation in terms of radius of gyration (R_g) and free power-law slope. In the second region, the medium q-range of 0.002 – 0.03 Å^{-1}, the intensity profile was dominated by the scattering from the individual nanoparticles. The scattering profiles in this region were fitted by utilizing the size-distribution model in modeling II [89]. Finally, in the high q-region (0.03 – 0.7 Å^{-1}), unified fit model ([91,92]) was employed. In the low q part of this region, a plateau is observed which defines a Guinier regime, therefore the size of the scatterers (in this case, the micropores and fractals) were also approximated along with the power-law profile. **Figure 1** is a schematic representation of these morphological features that correspond to the combined USAXS/SAXS data.

The changes in the short- and long-range bond order in silica nanoparticles that correspond to the observed microstructural features were probed using the pair distribution function (PDF) analysis from total X-ray scattering measurements. These data were acquired during the *in-operando* thermal treatment of silica nanoparticles up to 600 °C. The total scattering experiments were performed at Sector 11 of APS at Argonne National Laboratory using beamline 11-ID-B. The total scattering from the sample was recorded at an amorphous silicon-based area detector, 2048 × 2048 pixel Perkin-Elmer [93] with a sample-to-detector distance of ~16 cm. Calibrations for sample to detector distance, beam energy, beam center and nonorthogonality were performed using a cerium dioxide (CeO_2) standard (NIST diffraction intensity standard set 467a) [94]. The measurements were performed with an X-ray energy and wavelength of 58.6 keV and 0.2113 Å, respectively. After background and Compton scattering corrections, the PDFs were obtained using the xPDFsuite software [95].

To evaluate changes in the chemical bonding during thermal treatment processes, infrared (IR) spectra were acquired in an Attenuated Total Reflection (ATR) mode using an Attenuated Total Reflection-Fourier Transform Infrared spectrometer (ATR-FTIR, Nicolet™ iS™ 10, Waltham, MA) for samples treated at different temperatures (100, 150, 200, 300, 400, 500 600, 1050 °C). The spectra were collected in the range of 4000–650 cm^{-1} with total number of 32 scans for each run. The changes in the weight % of the silica nanoparticles during heat treatment were evaluated up to 600 °C and 955 °C for calcination and sintering, respectively, with a ramp rate of 5 °C/min in an N_2 environment (purged at 25 mL/min) using a Thermogravimetric Analyzer (TGA, TA Instruments, Q550, New Castle, DE). Additionally, the pore size distribution and specific surface areas of silica nanoparticles were determined using the nonlocal density functional theory (NLDFT, Quantachrome NOVAtouch Analyzer, Boynton Beach, FL) by 77 K N_2 adsorption. These measurements coupled with the X-ray scattering data provided detailed insights into the evolution of the pore morphology during the calcination and sintering processes. Untreated, calcined, and sintered silica nanoparticles were also imaged using a scanning electron microscope (Hitachi S3400 VP-SEM).

3. Results and Discussion

3.1 Evolution of Pore Morphology during the Calcination Process

The synthesis of model architected materials from spherical silica nanoparticles is a two-step process in which the particles are calcined at temperatures of 600 °C followed by sintering. The rationale for this approach is that calcination removes the functional groups such as ethoxy groups, and adsorbed water and NH_3 that may remain after the colloidal synthesis of these materials [96]. Sintering of these materials then could yield the interlinked nanoparticles with the micropore morphology representative of the geo-architected materials. The limited understanding of the *in-operando* evolution of the morphologies of these materials motivate the use of non-invasive cross-scale characterization of the morphologies of these materials using Ultra Small and Small Angle X-Ray Scattering (USAXS/SAXS) measurements. The USAXS/SAXS experimental data during the calcination process is presented in **Figure 2**. During the ramp to calcination temperature (**Figure 2 (a))**, the intensity of the scattering curves (at $q > 10^{-1}$ Å^{-1}) increases with temperature suggesting an increase in the number of scattering objects in this q regime [97].

However, during the isothermal heating at 600 °C, the calcination step, no significant changes in the scattering curves were noted. Additionally, the peak in the higher q-region at q = 1.45 Å^{-1} which corresponds to the (100) atomic plane in SiO_2 and d-spacing of 4.32 Å remained almost unchanged during the calcination stage [64]. As explained earlier, the experimental USAXS/SAXS data were modeled using the Modeling II tool in Irena program [89]. Representative fits for different SiO_2 nanoparticle samples are presented in **Figure S1**. To describe briefly, in the low q-region (<0.002 Å^{-1}), where no Guinier plateau regime is observed, the power-law exponents were obtained by setting the G value to zero [97] and keeping the power-law exponent as a free fitting parameter. It can be seen from **Figure 2** that scattering in this region does not change significantly and no appreciable changes in the power-law values were noted as presented in **Figure S2**. Therefore, the information from this region is not discussed further. In the medium q-region (0.002 – 0.03 Å^{-1}), the effect of thermal treatment on the size of individual nanoparticles was approximated by particle size distribution model. Gaussian type distribution was used to fit the model while utilizing the form factor of spheroid (aspect ratio = 1). In addition to the form factor, a structure factor for hard spheres was also incorporated in the approximation to fit the scattering profiles in the low q regime of this region. Particle radius and volume fraction were set as free parameters for approximation in this range. Finally, the unified fit model was used to approximate the scattering features in the high q-region (0.03 – 0.7 Å^{-1}). The plateau in this regime was fitted with a Guinier fit and the following higher q-range was approximated by the power-law exponent. The radius of gyration (R_g) obtained from the Guinier regime provided insights into the sizes of the nanometer sized pores in the nanoparticles while the power-law exponent provided information about the fractals present at the pore-solid interface ([91,92]). Additional details regarding Modeling II and complementary microstructural modeling fits are described by Ilavsky and Jemian ([86,89,97]) and Lee and co-workers [84].

The particle size volume fraction distribution and power-law slopes obtained from the modeling of experimental data during the calcination step are presented in **Figure 3**. The average size (radius) of nanoparticles slightly decreased from 127 nm to 122 nm during heating to calcination **Figure 3 (a-1)**. The spherical morphologies of these particles are noted from the SEM images of the untreated and calcined silica particles shown in the insets of **Figures 3 (a-1)** and (**a-2)**, respectively.

Analyses of the morphological features in the q-region of 0.03 – 0.7 Å^{-1} showed that the representative pore dimension of the spherical particles is to the order of 2.3 nm and does not change significantly during the calcination process. Further, the power law slopes determined from the unified fit tool show that the changes in the pore-solid interfaces decreases from 2.9 to 2.35 on heating from 35 °C to 600 °C, which corresponds to dehydroxylation ([96,98–100]). These mass fractal features are representative of pore-solid features in analogous siliceous materials [101].

The USAXS/SAXS experimental data were compared with N_2 adsorption-desorption measurements for untreated, calcined and SiO_2 nanoparticles treated at 150, 300, 400, and 500 °C. The measured N_2 adsorption-desorption isotherms are presented in **Figure S5**. The N_2 adsorption isotherms were modeled to obtain the pore size distribution and cumulative pore volumes for the SiO_2 nanoparticles using the NLDFT model in Quantachrome software using silica as the adsorbent by 77 K N_2 adsorption. The NLDFT modeling provided information about the micro- and mesopores (up to 16 nm) in the nanoparticles. The pore size distribution and cumulative pore volume data are presented in **Figure 4** for untreated and calcined SiO_2 nanoparticles and **Figure S5** for nanoparticles treated at 150, 300, 400, and 500 °C. The dominance of the pores with radii to the order of 2 nm is consistent with the USAXS/SAXS analyses. It can be noted in **Figure 4** and **Figure S5** that the amount of micropores slightly decrease during and after calcination, whereas the cumulative pore volume almost remained constant. The surface areas of the samples were also obtained from the NLDFT model and are reported in **Figure S7**. It was noted that the surface area of the particles decreased from 22.184 m^2/g to 19.282 m^2/g as a result of calcination.

The chemical changes that correspond to these morphological features were determined using ATR-FTIR spectra analyses. The morphological changes that correspond to temperatures in range of 25 - 600 °C are associated with the dehydroxylation of SiO_2 nanoparticles as indicated by the changes in Si-OH bond around 950 cm^{-1} in the ATR-FTIR spectra (**Figure 5**). Moreover, the changes in the Si-OH bond observed in IR spectra were related with the % weight changes due to dehydroxylation during calcination as determined by TGA measurements (**Figure S2**). A weight loss of about 8.5% was noted for silica nanoparticles as a result of heating to 600 °C.

We also performed total X-ray scattering experiments to obtain the pair distribution functions (PDFs) of silica nanoparticles during the calcination process. The PDF of a material describes its distribution and density of atomic distances ([102,103]). PDF can be obtained directly from the total X-ray scattering data by applying a Fourier transform on the reduced structure function S(Q), where Q is the scattering vector. The structure function is related to the PDF (G(r)) directly by:

$$G(r) = 4\pi r\,(\rho(r) - \rho_o) = {}^{2}/_{\pi} \int_0^{\infty} Q[S(Q) - 1]\sin(Qr)\,dQ \qquad (5)$$

where r is the interatomic distance, ρ(r) is the microscopic pair density and ρ_o is the average atomic density of the material ([103,104]).

The PDFs of SiO_2 nanoparticles on heating to the calcination temperature of 600 °C are shown in **Figure 6**. The complete dataset for *in-operando* PDFs is presented in **Figure S4**. In **Figure 6**, the oscillations before the Si-O peak and the two small peaks between the Si-O and O-O peaks are the termination ripples, a common feature in experimental PDF data, which appears as a consequence of limited Q range and instrumental contributions [102]. In **Figure 6**, we noted that the peak originating from the Si-O interactions observed around 1.61 Å shifted to a slightly smaller bond distance of 1.59 Å after heating to 600 °C. Similarly, the peak for Si-Si interactions noted at 3.08 Å initially became broader during heating and eventually shifted to relatively small value of 2.98 Å. It is well understood that the surface of silica contains silanol (Si-OH) groups ([96,100]) which can be removed upon thermal treatment at temperatures higher than 400 °C through a process called dehydroxylation. During this process, the one OH group and one hydrogen from the adjacent silanol bonds break away to form water as a result of a condensation reaction thus, giving rise to a siloxane Si-O-Si bridge [96]. The schematic representing this process is shown in the inset of **Figure 6** These chemical changes could be a reason of shift and broadening in the Si-O bond peak (**Figure 6**) with increasing temperature. This change in bond lengths for Si-O bond in the first shell could also affect the bond lengths for O-O and Si-Si as noted from our results.

3.2 Evolution of Pore Morphology during the Sintering Process

To investigate how sintering influences the morphology of the SiO_2 nanoparticles, the USAXS/SAXS experiments were performed in two stages. In the first stage, USAXS/SAXS data were collected as the temperatures were ramped from 35 °C to 1050 °C at a rate of 5 °C/min (**Figure 7**). During heating to the temperature of 1050 °C (**Figure 7** (**a**)), slight increase in the scattering intensity was observed in the q-range of 0.002 – 0.03 Å^{-1} until 917 °C. However, in the q-range of 0.03 – 0.7 Å^{-1}, the scattering intensity was observed to be decreasing significantly after 780 °C. This reduction in the scattering intensity could be associated with the decreasing sizes and number of pores during the sintering process. Similar decreasing trends in the scattering intensity during isothermal sintering at 1050 °C were observed for the first 90 minutes after which the scattering intensity almost became constant. Additionally, the diffraction peak at q = 1.45 Å^{-1} (4.32 Å) for (100) plane [64] in SiO_2 remained unchanged during the sintering process.

The modeled USAXS/SAXS data during the sintering process are presented in **Figure 8**. Moreover, the particle size volume distribution became narrow and relatively higher after 917 °C (**Figure 8 (a-1)**) with the peak center shifted from 125 nm to 120 nm during isothermal sintering at 1050 °C, the volume fraction distribution remained narrow with the peak center shifted to 118 nm (**Figure 8 (a-2)**). This change in the particle size distribution could be related with the scattering intensity trends discussed earlier and observed in the q-range of 0.002 – 0.03 Å^{-1} (**Figure 7**).

Furthermore, an increasing trend in values of power-law slope was observed after 917 °C during the heating step (see the red curve in **Figure 8 (b-1)**). The power-law slope changed slightly from 2.54 to 2.61 during heating from 35°C to 917 °C, however, it achieved the value of 2.73 after heating to 1050 °C. As a result of the isothermal sintering at 1050 °C, the power-law slope finally achieved the value of 2.88 (see the red curve in **Figure 8 (b-2)**). The values of power-law slopes indicated the presence of mass fractals at the pore-solid interface within the nanoparticles. This increase in the power-law slope for mass fractals indicated the emergence of relatively rougher interfaces ([105,106]). The R_g values, corresponding to the pore sizes, remained almost constant up to 800 °C and decreased on further heating to 1050 °C (see the black curve in **Figure 8(b-1)**).

The N_2 adsorption-desorption isotherms were also obtained for the sintered SiO_2 nanoparticles and are presented in **Figure 9**. The adsorption isotherm was modeled to obtain the pore size distribution and cumulative pore volume using the NLDFT model as explained earlier. It can be noted from **Figure 4**, **Figure 9** and **Figure S5** that the both the cumulative pore volume and number of micropores decrease significantly after the sintering process. Additionally, the surface area of sintered nanoparticles was measured to be 13.005 m^2/g as compared to 22.184 m^2/g and 19.282 m^2/g for untreated and calcined nanoparticles, respectively. The dominance of pores with radius of ~ 2 nm was observed in N_2 adsorption measurements, which agreed well with the X-ray scattering data.

The changes in the pore sizes on heating above 800 °C corresponded to the complete dehydroxylation of SiO_2 nanoparticles (> 800 °C) [96]. The weight loss caused by dehydroxylation was also observed in the TGA curve of calcined nanoparticles during sintering (**Figure S3**). This observation was also confirmed by the IR spectrum of the sintered nanoparticles where the vibrations from Si-OH band completely diminished as a result of sintering (**Figure 10)**. During the isothermal sintering stage at 1050 °C, the R_g values slightly increased in the first 100 minutes and then remained almost constant till the end of the stage (see the black curve in **Figure 8 (b-2)**).

Based on the changes in the pore dimensions and the corresponding chemical phenomena ([96,98–100]), a mechanism for the changes in the pore-solid interfaces can be developed. Dehydroxylation of the silanol groups (Si-OH) present on the silica surface yield Si-O-Si siloxane bridges ([96,100]) (see inset of **Figure 6)**. Residual Si-OH groups persist after calcination as presented in the ATR-FTIR spectra (**Figure 5**) and TGA data (**Figure S3**). The removal of these residual groups occurs during the secondary dehydroxylation stage at the temperatures higher than 800 °C.

Governed by the breaking and formation of new bonds at high temperatures, the proposed mechanism is presented in the **Figure 11**. Briefly, during heating to sintering step at temperatures higher than 800 °C, the new siloxane bridges (Si-O-Si) forming inside the pores at the pore-solid interface as a result of secondary dehydroxylation could give rise to rougher pore-solid interfaces (as noted from the power-law slope (red curve shown in **Figures 8 (b-1) and 8 (b-2))** and a decrease in the internal pore dimensions. These chemical changes could describe the abrupt decrease in the R_g values from 2.25 nm to 1.84 nm during the heating to sintering step after 800 °C. Furthermore, during the isothermal sintering at 1050 °C, a slight increase in the R_g value (1.98 nm) was noted until the first 90 minutes and remained almost constant during the rest of the sintering stage and finally achieved the value of 2 nm at the end of sintering. This increase in the pore dimensions during the sintering process could be explained by the merging of different pores. Since the USAXS/SAXS signals represent the average scattering from scatterers (in this case pores), the increase in the R_g values could be associated with the increase in the average value.

4. Conclusions

We present an experimental methodology to elucidate thermally induced morphological evolution during the calcination and sintering of silica nanoaprticles, and the underlying chemical changes associated with these morphological features. The hierarchical morphological organization is captured using USAXS/SAXS measurements. The results of the pore size of the samples on sintering from USAXS/SAXS measurements were quantitatively in good agreement with those obtained from N_2-adsorption measurements (NLDFT method). Changes in the short-range bond order during the calcination process are determined using total X-ray scatteirng measurements. The underlying changes in the hydroxylation conditions of silica are captured using ATR-FTIR measurements. Based on the observations from these measurements, a chemo-morphological mechanism that corresponds to the thermal treatment of spherical silica nanoparticles is presented.

On heating to the calcination temperature (600 °C), the power-law slope changed from around 2.9 to 2.45, indicating the transition of the pore-solid interface from rough to smooth as a result of dehydroxylation. However, during calcination at 600 °C, no significant changes at the pore-solid interface and R_g were observed, indicating the dehdroxylation of surface silanol groups during this step. Furthermore, during heating of calcined nanoparticles to sintering temperatures as high as 1050 °C, a decrease in the pore size was noted as the temperatures exceeded 800 °C. This decrease was attributed to the formation of Si-O-Si bridges inside the pores as a result of dehydroxylation. Isothermal sintering of the calcined nanoparticles at 1050 °C showed the emergence of slightly large size pore dimensions to the order of 2 nm from as compared to 1.8 nm pores noted at the beginning of sintering step. These morphological insights gleaned from rapid *in-operando* multi-scale scattering measurements are useful in advancing predictive controls on the synthesis of siliceous materials for a wide range of scientific and engineering applications.

Supporting Information

Plots of fitted models. Power-law slope values at low q region (< 0.002 Å^{-1}). TGA curves during calcination and sintering processes. Complete PDF dataset. N_2 adsorption-desorption isotherms. Pore size distribution and cumulative pore volumes of SiO_2 nanoparticles at 150, 300, 400, and 500 °C. NLDFT surface area of different SiO_2 nanoparticles.

Acknowledgments

This work was supported as part of the EFRC-MUSE, an Energy Frontier Research Center funded by the U.S. Department of Energy, Office of Science, Basic Energy Sciences under Award #DE-SC0019285. We would like to acknowledge the help provided by Dr. Jan Ilavsky, and Dr. Matthew Frith during the experiments at the USAXS facility, X-ray Science Division, Argonne National Laboratory. The use of the Advanced Photon Source, an Office of the Science User Facility operated for the U.S. Department of Energy (DOE) Office of Science by Argonne National Laboratory, is supported by the U.S. DOE under Contract DE-AC02-06CH11357.

References

[1] E. Barsotti, S.P. Tan, S. Saraji, M. Piri, J. Chen, A Review on Capillary Condensation in Nanoporous Media: Implications for Hydrocarbon Recovery from Tight Reservoirs, Fuel. 184 (2016) 344–361. doi:10.1016/j.fuel.2016.06.123.

[2] M. Pathak, H. Cho, M. Deo, Experimental and Molecular Modeling Study of Bubble Points of Hydrocarbon Mixtures in Nanoporous Media, Energy & Fuels. 31 (2017) 3427–3435. doi:10.1021/acs.energyfuels.6b02422.

[3] M. Alfi, H. Nasrabadi, D. Banerjee, Experimental Investigation of Confinement Effect on Phase Behavior of Hexane, Heptane and Octane using Lab-on-a-Chip Technology, Fluid Phase Equilib. 423 (2016) 25–33. doi:10.1016/j.fluid.2016.04.017.

[4] H. Cho, D. Caputo, M.H. Bartl, M. Deo, Measurements of Hydrocarbon Bubble Points in Synthesized Mesoporous Siliceous Monoliths, Chem. Eng. Sci. 177 (2018) 481–490. doi:10.1016/j.ces.2017.12.005.

[5] H. Cho, M.H. Bartl, M. Deo, Bubble Point Measurements of Hydrocarbon Mixtures in Mesoporous Media, Energy & Fuels. 31 (2017) 3436–3444. doi:10.1021/acs.energyfuels.6b02424.

[6] Z. Jin, A. Firoozabadi, Phase Behavior and Flow in Shale Nanopores from Molecular Simulations, Fluid Phase Equilib. 430 (2016) 156–168. doi:10.1016/j.fluid.2016.09.011.

[7] P. Kumar, S. V Buldyrev, F.W. Starr, N. Giovambattista, H.E. Stanley, Thermodynamics, Structure, and Dynamics of Water Confined between Hydrophobic Plates, Phys. Rev. E. 72 (2005) 051503. doi:10.1103/PhysRevE.72.051503.

[8] T. Le, A. Striolo, C.H. Turner, D.R. Cole, Confinement Effects on Carbon Dioxide Methanation: A Novel Mechanism for Abiotic Methane Formation, Sci. Rep. 7 (2017) 9021. doi:10.1038/s41598-017-09445-1.

[9] D. Feng, X. Li, X. Wang, J. Li, T. Zhang, Z. Sun, M. He, Q. Liu, J. Qin, S. Han, Capillary Filling of Confined Water in Nanopores: Coupling the Increased Viscosity and Slippage, Chem. Eng. Sci. 186 (2018) 228–239. doi:10.1016/j.ces.2018.04.055.

[10] C. Iacob, J.R. Sangoro, W.K. Kipnusu, R. Valiullin, J. Karger, F. Kremer, Enhanced Charge Transport in Nano-Confined Ionic Liquids, Soft Matter. 8 (2012) 289–293. doi:10.1039/c1sm06581e.

[11] Y. Liu, Q. Wang, T. Wu, L. Zhang, Fluid Structure and Transport Properties of Water Inside Carbon Nanotubes, J. Chem. Phys. 123 (2005) 234701. doi:10.1063/1.2131070.

[12] Y. Liu, Q. Wang, L. Lu, Transport Properties and Distribution of Water Molecules Confined in Hydrophobic Nanopores and Nanoslits, Langmuir. 20 (2004) 6921–6926. doi:10.1021/la036325l.

[13] M. Fasano, E. Chiavazzo, P. Asinari, Water Transport Control in Carbon Nanotube Arrays, Nanoscale Res. Lett. 9 (2014) 559.

[14] Y. Zhang, W. Yu, K. Sepehrnoori, Y. Di, Investigation of Nanopore Confinement on Fluid Flow in Tight Reservoirs, J. Pet. Sci. Eng. 150 (2017) 265–271. doi:10.1016/j.petrol.2016.11.005.

[15] C.H. Turner, J.K. Johnson, K.E. Gubbins, Effect of Confinement on Chemical Reaction Equilibria: The Reactions $2NO \rightarrow (NO)_2$ and $N_2 + 3H_2 <-> 2NH_3$ in Carbon Micropores, J. Chem. Phys. 114 (2001) 1851–1859. doi:10.1063/1.1328756.

[16] C.H. Turner, J.K. Brennan, J. Pikunic, K.E. Gubbins, Simulation of Chemical Reaction Equilibria and Kinetics in Heterogeneous Carbon Micropores, Appl. Surf. Sci. 196 (2002) 366–374.

[17] T. Xu, J.A. Apps, K. Pruess, Reactive Geochemical Transport Simulation to Study Mineral Trapping for CO2 Disposal in Deep Arenaceous Formations, J. Geophys. Res. 108 (2003) 2071. doi:10.1029/2002JB001979.

[18] X.Q. Cheng, Y.L. Zhang, Z.W. Wang, Z.H. Guo, Y.P. Bai, L. Shao, Recent Advances in Polymeric Solvent-Resistant Nanofiltration Membranes, Adv. Polym. Technol. 33 (2014) 21455.

[19] A.W. Mohammad, Y.H. Teow, W.L. Ang, Y.T. Chung, D.L. Oatley-radcliffe, N. Hilal, Nano Filtration Membranes Review: Recent Advances and Future Prospects, Desaination. 356 (2015) 226–254. doi:10.1016/j.desal.2014.10.043.

[20] S. Faucher, N. Aluru, M.Z. Bazant, D. Blankschtein, A.H. Brozena, J. Cumings, J.P. De Souza, M. Elimelech, R. Epsztein, J.T. Fourkas, A.G. Rajan, H.J. Kulik, A. Levy, A. Majumdar, C. Martin, M. Mceldrew, R.P. Misra, A. Noy, T.A. Pham, M. Reed, E. Schwegler, Z. Siwy, Y. Wang, M. Strano, Critical Knowledge Gaps in Mass Transport through Single-Digit Nanopores: A Review and Perspective, J. Phys. Chem. C. XXXX (2019) XXX–XXX. doi:10.1021/acs.jpcc.9b02178.

[21] K.P. Lee, T.C. Arnot, D. Mattia, A Review of Reverse Osmosis Membrane Materials for Desalination — Development to Date and Future Potential, J. Memb. Sci. 370 (2011) 1–22. doi:10.1016/j.memsci.2010.12.036.

[22] M.E. Davis, Ordered Porous Materials for Emerging Applications, Nature. 417 (2002) 813–821.

[23] X. Liu, D. Zhang, A Review of Phase Behavior Simulation of Hydrocarbons in Confined Space: Implications for Shale Oil and Shale Gas, J. Nat. Gas Sci. Eng. 68 (2019) 102901. doi:10.1016/j.jngse.2019.102901.

[24] N. Tyler, R.J. Finley, Architectural Controls on the Recovery of Hydrocarbons from Sandstone Reservoirs, Three Dimens. Facies Archit. Heterog. Clastic Sediments Its Implic. Hydrocarb. Discov. Recover. Concepts Sedimentol. Paleontol. 3 (1991) 44–54.

[25] H. Singh, A Critical Review of Water Uptake by Shales, J. Nat. Gas Sci. Eng. 34 (2016) 751–766. doi:10.1016/j.jngse.2016.07.003.

[26] M. Abdul, Q. Siddiqui, S. Ali, H. Fei, H. Roshan, Current Understanding of Shale Wettability: A Review on Contact Angle Measurements, Earth-Science Rev. 181 (2018) 1–11. doi:10.1016/j.earscirev.2018.04.002.

[27] Z. Sun, Y. Kang, Y. Kang, Confinement-Induced Modulation of Elastic Properties of Nano-Confined Fluids in Slit Pore, Chin. Phys. B. 28 (2019) 036102. doi:10.1088/1674-1056/28/3/036102.

[28] P. Jean-christophe, B. Sally, An Experimental Study on the Influence of Sub-Core Scale Heterogeneities on CO_2 Distribution in Reservoir Rocks, Transp. Porous Media. 82 (2010) 93–109. doi:10.1007/s11242-009-9426-x.

[29] S. Krevor, M.J. Blunt, S.M. Benson, C.H. Pentland, C. Reynolds, A. Al-menhali, B. Niu, Capillary Trapping for Geologic Carbon Dioxide Storage – From Pore Scale Physics to Field Scale Implications, Int. J. Greenh. Gas Control. 40 (2015) 221–237.

doi:10.1016/j.ijggc.2015.04.006.

[30] S.M. Benson, T. Surles, Carbon Dioxide Capture and Storage: An Overview With Emphasis on Capture and Storage in Deep Geological Formations, Proc. IEEE. 94 (2006) 1795–1805.

[31] D. Silin, L. Tomutsa, T. Patzek, S. Benson, Microtomography and Pore-Scale Modeling of Two-Phase Fluid Distribution, Transp. Porous Media. 86 (2011) 495–515.

[32] J.A. de Chalendar, C. Garing, S.M. Benson, Pore-Scale Considerations on Ostwald Ripening in Rocks, Energy Procedia. 114 (2017) 4857–4864. doi:10.1016/j.egypro.2017.03.1626.

[33] C.M. Oldenburg, K. Pruess, S.M. Benson, Process Modeling of CO_2 Injection into Natural Gas Reservoirs for Carbon Sequestration and Enhanced Gas Recovery, Energy & Fuels. 15 (2001) 293–298. doi:10.1021/ef000247h.

[34] S.C.M. Krevor, R. Pini, L. Zuo, S.M. Benson, Relative Permeability and Trapping of CO_2 and Water in Sandstone Rocks at Reservoir Conditions, Water Resour. Res. 48 (2012) W02532. doi:10.1029/2011WR010859.

[35] K. Rasmusson, M. Rasmusson, Y. Tsang, S. Benson, F. Hingerl, F. Fagerlund, A. Niemi, Residual trapping of carbon dioxide during geological storage — Insight gained through a pore-network modeling approach, Int. J. Greenh. Gas Control. 74 (2018) 62–78. doi:10.1016/j.ijggc.2018.04.021.

[36] A. Aminian, B. Zarenezhad, Oil-Detachment from the Calcium Carbonate Surfaces via the Actions of Surfactant, Nanoparticle and Low Salinity Brine: An Insight from Molecular Dynamic Simulation, Chem. Eng. Sci. 202 (2019) 373–382. doi:10.1016/j.ces.2019.03.031.

[37] S. Yuan, S. Wang, X. Wang, M. Guo, Y. Wang, D. Wang, Molecular Dynamics Simulation of Oil Detachment from Calcite Surface in Aqueous Surfactant Solution, Comput. Theor. Chem. 1092 (2016) 82–89. doi:10.1016/j.comptc.2016.08.003.

[38] J. Zhao, G. Yao, S.B. Ramisetti, R.B. Hammond, D. Wen, Molecular Dynamics Investigation of Substrate Wettability Alteration and Oil Transport in a Calcite Manopore, Fuel. 239 (2019) 1149–1161. doi:10.1016/j.fuel.2018.11.089.

[39] B.J. Bucior, D. Chen, J. Liu, J.K. Johnson, Porous Carbon Nanotube Membranes for Separation of H_2/CH_4 and CO_2/CH_4 Mixtures, J. Phys. Chem. C. 116 (2012) 25904–25910. doi:10.1021/jp3098022.

[40] B. Kueh, M. Kapsi, C.M. Veziri, C. Athanasekou, G. Pilatos, K.S.K. Reddy, A. Raj, G.N. Karanikolos, Asphaltene-Derived Activated Carbon and Carbon Nanotube Membranes for CO_2 Separation, Energy & Fuels. 32 (2018) 11718–11730. doi:10.1021/acs.energyfuels.8b02913.

[41] G. Yi, S. Chen, X. Quan, G. Wei, X. Fan, H. Yu, Enhanced Separation Performance of Carbon Nanotube–Polyvinyl Alcohol Composite Membranes for Emulsified Oily Wastewater Treatment under Electrical Assistance, Sep. Purif. Technol. 197 (2018) 107–115. doi:10.1016/j.seppur.2017.12.058.

[42] J. Gu, P. Xiao, J. Chen, J. Zhang, Y. Huang, T. Chen, Janus Polymer/Carbon Nanotube

Hybrid Membranes for Oil/Water Separation, ACS Appl. Mater. Interfaces. 6 (2014) 16204–16209. doi:10.1021/am504326m.

[43] M. Jin, G. Zhang, Z. Guo, Z. Lv, Tungsten Doped Mesoporous SBA-16 as Novel Heterogeneous Catalysts for Oxidation of Cyclopentene to Glutaric Acid, Appl. Organomet. Chem. 32 (2018) 4317.

[44] V.K. Tomer, S. Duhan, R. Malik, S.P. Nehra, S. Devi, A Novel Highly Sensitive Humidity Sensor Based on ZnO/SBA-15 Hybrid Nanocomposite, J. Am. Ceram. Soc. 98 (2015) 3719–3726. doi:10.1111/jace.13836.

[45] O. Josypcuk, M. Fojta, A. Danhel, B. Josypcuk, Applying Mesoporous Silica SBA-15 in Electrochemical Detection of DNA Hybridization, Electroanalysis. 28 (2016) 1860–1864. doi:10.1002/elan.201501137.

[46] P. Zhang, Z. Wu, T. Liu, Z. Li, High-Temperature Synthesis of Ordered Hexagonal Mesoporous Silica Materials (SBA-15) with Adjustable Large Mesopores for Selective Adsorption of Biomolecules, Eur. J. Inorg. Chem. (2014) 5577–5584. doi:10.1002/ejic.201402511.

[47] C. Wen, S. Li, S. Zeng, Z. Zhang, S.-L. Zhang, Autogenic Analyte Translocation in Nanopores, Nano Energy. 60 (2019) 503–509. doi:10.1016/j.nanoen.2019.03.092.

[48] P. Xie, Q. Xiong, Y. Fang, Q. Qing, C.M. Lieber, Local Electrical Potential Detection of DNA by Nanowire–Nanopore Sensors, Nat. Nanotechnol. 7 (2012) 119–125. doi:10.1038/nnano.2011.217.

[49] T.J. Morin, T. Shropshire, X. Liu, K. Briggs, C. Huynh, V. Tabard-, H. Wang, W.B. Dunbar, Nanopore-Based Target Sequence Detection, PLoS One. (2016) 1–21. doi:10.1371/journal.pone.0154426.

[50] S. Cai, J.Y.Y. Sze, J.B. Edel, Small Molecule Electro-Optical Binding Assay using Nanopores, Nat. Commun. 10 (2019) 1797. doi:10.1038/s41467-019-09476-4.

[51] F. Al-Dirini, M.A. Mohammed, M.S. Hossain, F.M. Hoassain, A. Nirmalathas, E. Skafidas, Tuneable Graphene Nanopores for Single Biomolecule Detection, Nanoscale. 8 (2016) 10066–10077. doi:10.1039/c5nr05274b.

[52] S. Dire, V. Tagliazucca, L. Salvadori, G.D. Soraru, Preparation of Dense and Porous Silicon Oxycarbide Submicrometer-Sized Spheres Using a Modified Sto˙ber Process, J. Am. Ceram. Soc. 94 (2011) 3819–3824.

[53] G.H. Bogush, M.A. Tracy, C.F. Zukoski IV, Preparation of Monodisperse Silica Particles: Control of Size and Mass Fraction, J. Non. Cryst. Solids. 104 (1988) 95–106.

[54] A.K. Bohaty, J.J. Smith, I. Zharov, Free-Standing Silica Colloidal Nanoporous Membranes, Langmuir. 25 (2009) 3096–3101.

[55] I. Zharov, A. Khabibullin, Surface-Modified Silica Colloidal Crystals: Controlled Ionic and Molecular Transport, Acc. Chem. Res. 47 (2014) 440–449. doi:10.1021/ar400157w.

[56] B. Zhao, C. Tian, Y. Zhang, T. Tang, F. Wang, Size Control of Monodisperse Nonporous

Silica Particles by Seed Particle Growth, Particuology. 9 (2011) 314–317. doi:10.1016/j.partic.2010.07.028.

[57] M. Meier, J. Ungerer, M. Klinge, H. Nirschl, Synthesis of Nanometric Silica Particles via a Modified Stöber Synthesis Route, Colloids Surfaces A. 538 (2018) 559–564. doi:10.1016/j.colsurfa.2017.11.047.

[58] S.L. Greasley, S.J. Page, S. Sirovica, S. Chen, R.A. Martin, A. Riveiro, J. V Hanna, A.E. Porter, J.R. Jones, Controlling Particle Size in the Stöber Process and Incorporation of Calcium, J. Colloid Interface Sci. 469 (2016) 213–223. doi:10.1016/j.jcis.2016.01.065.

[59] Y. Takeda, Y. Komori, H. Yoshitake, Direct Stöber Synthesis of Monodisperse Silica Particles Functionalized with Mercapto-, Vinyl- and Aminopropylsilanes in Alcohol – Water Mixed Solvents, Colloids Surfaces A Physicochem. Eng. Asp. 422 (2013) 68–74. doi:10.1016/j.colsurfa.2013.01.024.

[60] E.G. Barrera, P.R. Livotto, J.H.Z. dos Santos, Hybrid Silica Bearing Different Organosilanes Produced by the Modified Stöber Method, Powder Technol. 301 (2016) 486–492. doi:10.1016/j.powtec.2016.04.025.

[61] X. Wang, Z. Shen, T. Sang, X. Cheng, M. Li, L. Chen, Z. Wang, Preparation of Spherical Silica Particles by Stöber Process with High Concentration of Tetra-Ethyl-Orthosilicate, J. Colloid Interface Sci. 341 (2010) 23–29. doi:10.1016/j.jcis.2009.09.018.

[62] R.S. Fernandes, I.M. Raimundo, M.F. Pimentel, Revising the Synthesis of Stöber Silica Nanoparticles: A Multivariate Assessment Study on the Effects of Reaction Parameters on the Particle Size, Colloids Surfaces A. 577 (2019) 1–7. doi:10.1016/j.colsurfa.2019.05.053.

[63] K. Nozawa, H. Gailhanou, L. Raison, P. Panizza, H. Ushiki, E. Sellier, J.P. Delville, M.H. Delville, Smart Control of Monodisperse Stober Silica Particles: Effect of Reactant Addition Rate on Growth Process, Langmuir. (2005) 1516–1523. doi:10.1021/la048569r.

[64] T. Gholami, M. Salavati-Niasari, M. Bazarganipour, E. Noori, Synthesis and Characterization of Spherical Silica Nanoparticles by Modified Stöber Process Assisted by Organic Ligand, Superlattices Microstruct. 61 (2013) 33–41. doi:10.1016/j.spmi.2013.06.004.

[65] Q. Guo, G. Yang, D. Huang, W. Cao, L. Ge, L. Li, Synthesis and Characterization of Spherical Silica Nanoparticles by Modified Stöber Process Assisted by Slow-Hydrolysis Catalyst, Colloid Polym. Sci. 2 (2018) 379–384.

[66] D.A. Kurdyukov, D.A. Eurov, D.A. Kirilenko, V. V Sokolov, V.G. Golubev, Tailoring the Size and Microporosity of Stober Silica Particles, Microporous Mesoporous Mater. 258 (2018) 205–210. doi:10.1016/j.micromeso.2017.09.017.

[67] S. Li, Q. Wan, Z. Qin, Y. Fu, Y. Gu, Unraveling the Mystery of Stöber Silica's Microporosity, Langmuir. 32 (2016) 9180–9187. doi:10.1021/acs.langmuir.6b02472.

[68] S. Li, Q. Wan, Z. Qin, Y. Fu, Y. Gu, Understanding Stöber Silicas Pore Characteristics Measured by Gas Adsorption, Langmuir. 31 (2015) 824–832. doi:10.1021/la5042103.

[69] C.J. Brinker, G.W. Scherer, Sol-Gel Science: The Physics and Chemistry of Sol-Gel

Processing, Academic Press, San Diego, 1990.

[70] I.A.M. Ibrahim, A.A.F. Zikry, M.A. Sharaf, Preparation of Spherical Silica Nanoparticles: Stober Silica, J. Am. Sci. 6 (2010) 985–989.

[71] K. Kim, J. Kim, W. Kim, Influence of Reaction Conditions on Sol-Precipitation Process Producing Silicon Oxide Particles, Ceram. Int. 28 (2002) 187–194.

[72] K.-S. Chou, C.-C. Chen, Preparation of Monodispersed Silica Colloids Using Sol-Gel Method: Cosolvent Effect, in: Innov. Process. Synhtesis Ceram. Glas. Compos. VIII, Vol. 166, n.d.

[73] H. Boukari, G.G. Long, M.T. Harris, Polydispersity during the Formation and Growth of the Stöber Silica Particles from Small-Angle X-ray Scattering Measurements, J. Colloid Interface Sci. 229 (2000) 129–139. doi:10.1006/jcis.2000.7007.

[74] S. Fouilloux, J. Daillant, A. Thill, Single Step Synthesis of 5–30 nm Monodisperse Silica Nanoparticles: Important Experimental Parameters and Modeling, Colloids Surfaces A Physicochem. Eng. Asp. 393 (2012) 122–127. doi:10.1016/j.colsurfa.2011.11.009.

[75] S. Fouilloux, A. Désert, O. Taché, O. Spalla, J. Daillant, A. Thill, SAXS Exploration of the Synthesis of Ultra Monodisperse Silica Nanoparticles and Quantitative Nucleation Growth Modeling, J. Colloid Interface Sci. 346 (2010) 79–86. doi:10.1016/j.jcis.2010.02.052.

[76] D.L. Green, J.S. Lin, Y.F. Lam, M.Z.C. Hu, D.W. Schaefer, M.T. Harris, Size, Volume fraction, and nucleation of Stober silica nanoparticles, J. Colloid Interface Sci. 266 (2003) 346–358. doi:10.1016/S0021-9797(03)00610-6.

[77] D.L. Green, S. Jayasundara, Y. Lam, M.T. Harris, Chemical Reaction Kinetics Leading to the First Stöber Silica Nanoparticles – NMR and SAXS Investigation, J. Non. Cryst. Solids. 315 (2003) 166–179.

[78] P. Dibandjo, L. Bois, C. Estournes, B. Durand, P. Miele, Silica , Carbon and Boron Nitride Monoliths with Hierarchical Porosity Prepared by Spark Plasma Sintering Process, Microporous Mesoporous Mater. 111 (2008) 643–648. doi:10.1016/j.micromeso.2007.07.036.

[79] B. Barazami, D. Torikai, Spark Plasma Sintering of Silica Glass: Experimental Study on the Temperature Distribution and Influence of the Heating Rate on Bubble Formation, Glas. Technol. Eur. J. Glas. Sci. Technol. Part A. 57 (2016) 89–94.

[80] M. Liu, G. Gadikota, Chemo-Morphological Coupling during Serpentine Heat Treatment for Carbon Mineralization, Fuel. 227 (2018) 379–385. doi:10.1016/j.fuel.2018.04.097.

[81] G. Gadikota, F. Zhang, A.J. Allen, Towards Understanding the Microstructural and Structural Changes in Natural Hierarchical Materials for Energy Recovery: In- operando Multi-Scale X-ray Scattering Characterization of Na- and Ca-Montmorillonite on Heating to 1150 ° C, (2017) 195–209. doi:10.1016/j.fuel.2017.01.092.

[82] M. Liu, G. Gadikota, Probing the Influence of Thermally Induced Structural Changes on the Microstructural Evolution in Shale using Multiscale X-ray Scattering Measurements, Energy and Fuels. 32 (2018) 8193–8201. doi:10.1021/acs.energyfuels.8b01486.

[83] J. Ilavsky, P.R. Jemian, A.J. Allen, F. Zhang, L.E. Levine, G.G. Long, Ultra-small-angle X-ray Scattering at the Advanced Photon Source, J. Appl. Crystallogr. 42 (2009) 469–479. doi:10.1107/s0021889809008802.

[84] T. Li, A.J. Senesi, B. Lee, Small Angle X-ray Scattering for Nanoparticle Research, Chem. Rev. 116 (2016) 11128–11180. doi:10.1021/acs.chemrev.5b00690.

[85] U. Bonse, M. Hart, Tailless X-ray Single-Crystal Reflection Curves Obtained by Multiple Reflection, Appl. Phys. Lett. 7 (1965) 238–240. doi:10.1063/1.1754396.

[86] J. Ilavsky, F. Zhang, A.J. Allen, L.E. Levine, P.R. Jemian, G.G. Long, Ultra-Small-Angle X-ray Scattering Instrument at the Advanced Photon Source: History , Recent Development, and Current Status, Metall. Matierals Trans. 44A (2013) 68–76. doi:10.1007/s11661-012-1431-y.

[87] M. Nyam-Osor, D.V. Soloviov, Y.S. Kovalev, A. Zhigunov, A.V. Rogachev, O.I. Ivankov, R.V. Erhan, A.I. Kuklin, Silver Behenate and Silver Stearate Powders for Calibration of SAS Instruments, J. Phys. Conf. Ser. 351 (2012) 012024. doi:10.1088/1742-6596/351/1/012024.

[88] J. Ilavsky, Nika: Software for Two- Dimensional Data Reduction, J. Appl. Crystallogr. 45 (2012) 324–326.

[89] J. Ilavsky, P.R. Jemian, Irena: Tool Suite for Modeling and Analysis of Small-Angle Scattering, J. Appl. Crystallogr. 42 (2009) 347–353.

[90] O. Glatter, O. Kratky, Small Angle X-ray Scattering, Academic Press, 1982.

[91] G. Beaucage, Approximations Leading to a Unified Exponential/Power-Law Approach to Small-Angle Scattering, J. Appl. Crystallogr. 28 (1995) 717–728.

[92] G. Beaucage, Small-Angle Scattering from Polymeric Mass Fractals of Arbitrary Mass-Fractal Dimension, J. Appl. Crystallogr. 29 (1996) 134–146. doi:10.1107/S0021889895011605.

[93] P.J. Chupas, K.W. Chapman, P.L. Lee, Applications of an Amorphous Silicon-Based Area Detector for High-Resolution, High-Sensitivity and Fast Time-Resolved Pair Distribution Function Measurements, J. Appl. Crystallogr. 40 (2007) 463–470. doi:10.1107/S0021889807007856.

[94] A. Hoeher, S. Mergelsberg, O.J. Borkiewicz, P.M. Dove, F.M. Michel, A New Method for in-situ Structural Investigations of Nano-Sized Amorphous and Crystalline Materials Using Mixed-Flow Reactors, Acta Crystallogr. Sect. A Found. Adv. A75 (2019) 758–765. doi:10.1107/S2053273319008623.

[95] X. Yang, P. Juhas, C.L. Farrow, S.J.L. Billinge, xPDFsuite: An End-to-End Software Solution for High throughput Pair Distribution Function Transformation, Visualization and Analysis, ArXiv 1402.3163. (2014) 1–4. http://arxiv.org/abs/1402.3163.

[96] L.T. Zhuravlev, The Surface Chemistry of Amorphous Silica. Zhuravlev model, Colloids Surfaces A Physicochem. Eng. Asp. 173 (2000) 1–38.

[97] A. Benedetti, J. Ilavsky, C. Segre, M. Strumendo, Analysis of Textural Properties of CaO-Based CO_2 Sorbents by ex-situ USAXS, Chem. Eng. J. 355 (2019) 760–776. doi:10.1016/j.cej.2018.07.164.

[98] L.T. Zhuravlev, Structurally Bound Water and Surface Characterization of Amorphous Silica, Pure Appl. Chem. 61 (1989) 1969–1976.

[99] L.T. Zhuravlev, Surface Characterization of Amorphous Silica: A Review of Work from the Former USSR, Colloids Surfaces A Physicochem. Eng. Asp. 74 (1993) 71–90.

[100] C.S. Ewing, S. Bhavsar, J.J. Mccarthy, J.K. Johnson, Accurate Amorphous Silica Surface Models from First-Principles Thermodynamics of Surface Dehydroxylation, Langmuir. 30 (2014) 5133–5141. doi:10.1021/la500422p.

[101] B.N. Nair, W.J. Elferink, K. Keizer, H. Verweij, Sol – Gel Synthesis and Characterization of Microporous Silica Membranes I: SAXS Study on the Growth of Polymeric Structures, J. Colloid Interface Sci. 178 (1996) 565–570.

[102] T. Proffen, S.J.L. Billinge, T. Egami, D. Louca, Structural Analysis of Complex Materials using the Atomic Pair Distribution Function - A Practical Guide, Z. Krist. 218 (2003) 132–143. doi:10.1524/zkri.218.2.132.20664.

[103] M.M. Martínez-Iñesta, I. Peral, T. Proffen, R.F. Lobo, A Pair Distribution Function Analysis for Zeolite Beta, Stud. Surf. Sci. Catal. 154 B (2004) 1393–1399. doi:10.1016/j.micromeso.2004.07.040.

[104] R.K. Biswas, P. Khan, S. Mukherjee, A.K. Mukhopadhyay, J. Ghosh, K. Muraleedharan, Study of Short Range Structure of Amorphous Silica from PDF using Ag Radiation in Laboratory XRD System, RAMAN and NEXAFS, J. Non. Cryst. Solids. 488 (2018) 1–9. doi:10.1016/j.jnoncrysol.2018.02.037.

[105] H. Asgar, S. Mohammed, I. Kuzmenko, G. Gadikota, Relating Structural and Microstructural Evolution to the Reactivity of Cellulose and Lignin during Alkaline Thermal Treatment with $Ca(OH)_2$ for Sustainable Energy Production Integrated with CO_2 Capture, ACS Sustain. Chem. Eng. 7 (2019) 5449–5461. doi:10.1021/acssuschemeng.8b06584.

[106] J. Ilavsky, F. Zhang, R.N. Andrews, I. Kuzmenko, P.R. Jemian, L.E. Levine, A.J. Allen, Development of Combined Microstructure and Structure Characterization Facility for in-situ and operando Studies at the Advanced Photon Source, J. Appl. Crystallogr. 51 (2018) 867–882. doi:10.1107/S160057671800643X.

Figure captions

Figure 1. Representative ultra-small and small angle X-ray scattering (USAXS/SAXS) experimental curve of SiO_2 nanoparticles. The curve is divided into three different regions which were modeled to obtain the information about the physical features of interest.

Figure 2. Ultra-small and small angle X-ray scattering (USAXS/SAXS) experimental data represent changes in the microstructural features of SiO_2 nanoparticles during heating to calcination temperature **(a)** and during calcination at 600 °C **(b)**.

Figure 3. Particle size volume fraction distributions of silica nanoparticles approximated in the q-range of 0.002-0.03 $Å^{-1}$ on heating to calcination temperature **(a-1)** and during the calcination process **(a-2)**. The changes in the pore morphology in the q-range of 0.03-0.7 $Å^{-1}$ as represented by the characteristic radius of gyration (Rg) (black curve) and the power-law slope (red curve) during the temperature ramp to achieve the calcination temperature (**b-1**) and at the calcination temperature (**b-2**). The error bars on R_g values and power-law slopes correspond to 3% of error in calculated values. The insets in **(a-1)** and **(a-2)** represent the corresponding scanning electron micrographs.

Figure 4. Pore size distributions and cumulative pore volumes of untreated **(a)**, and calcined **(b)** silica nanoparticles. SiO_2 nanoparticles were prepared by the modified Stöber method and calcined at 600 °C for 4 hours.

Figure 5. Changes in the Si-OH and Si-O-Si features for SiO_2 nanoparticles heated to different temperatures and calcined at 600 °C measured using Attenuated Total Reflectance Fourier Transform Infrared Spectroscopy (ATR-FTIR). Bands around 795 cm^{-1}, 950 cm^{-1}, and 1054 cm^{-1} correspond to Si-O-Si (sym.), Si-OH, and Si-O-Si (asym.) vibrations, respectively. With an increase in temperature, the Si-O-Si asymmetric band broadens while Si-OH vibration band ~950 cm^{-1} appears to be diminished in the calcined sample as a result of dehydroxylation of silica.

Figure 6. The pair distribution function (PDF) curves calculated from total X-ray scattering data during the in-operando heating of silica nanoparticles to calcination temperature (600 °C). Inset shows the schematic of dehydroxylation process i.e., breakage of silanol (Si-OH) bonds and formation of new siloxane (Si-O-Si) bridges.

Figure 7. Ultra-small and small angle X-ray scattering (USAXS/SAXS) experimental data represent changes in the microstructural features of calcined SiO_2 nanoparticles during heating to sintering temperature **(a)** and during sintering at 1050 °C **(b)**.

Figure 8. Particle size volume fraction distributions of calcined silica nanoparticles on heating to the sintering temperature **(a-1)** and during the sintering process **(a-2)** approximated in the q-range of 0.002-0.03 $Å^{-1}$. The changes in the pore morphology in the q-range of 0.03-0.7 A^{-1} as represented by the characteristic radius of gyration (Rg) (black curve) and the power-law slope (red curve) during the temperature ramp to achieve sintering temperature (**b-1**) and at the sintering temperature (**b-2**). The error bars on R_g and power-law values correspond to 3% of error in calculated values. The inset in **(a-2)** represent the corresponding scanning electron micrograph.

Figure 9. Pore size distribution and cumulative pore volume of sintered SiO_2 nanoparticles. SiO_2 nanoparticles were prepared by modified Stöber method, calcined at 600 °C for 4 hours and sintered at 1050 °C for 4 hours.

Figure 10. Comparison of changes in the Si-OH and Si-O-Si features for untreated, calcined and sintered SiO_2 nanoparticles measured using Attenuated Total Reflectance Fourier Transform Infrared Spectroscopy (ATR-FTIR). Bands around 795 cm^{-1}, 950 cm^{-1}, and 1054 cm^{-1} correspond to Si-O-Si (sym.), Si-OH, and Si-O-Si (asym.) vibrations, respectively. With an increase in temperature, the Si-O-Si asymmetric band broadens while Si-OH vibration band ~950 cm^{-1} diminishes completely as a result of sintering at 1050 °C.

Figure 11. Schematic representation of chemo-morphological changes that occurring during sintering of silica nanoparticles. As a result of heating to calcination temperature (600 °C), primary dehydroxylation of -OH groups from silanol (Si-OH) bonds generate siloxane (Si-O-Si) bridges (change from **I** to **II**). Heating the calcined nanoparticles to sintering temperature (1050 °C) results in secondary dehydroxylation, which starts after 800 °C where Si-O-Si bridges could form inside the pores (**III**).

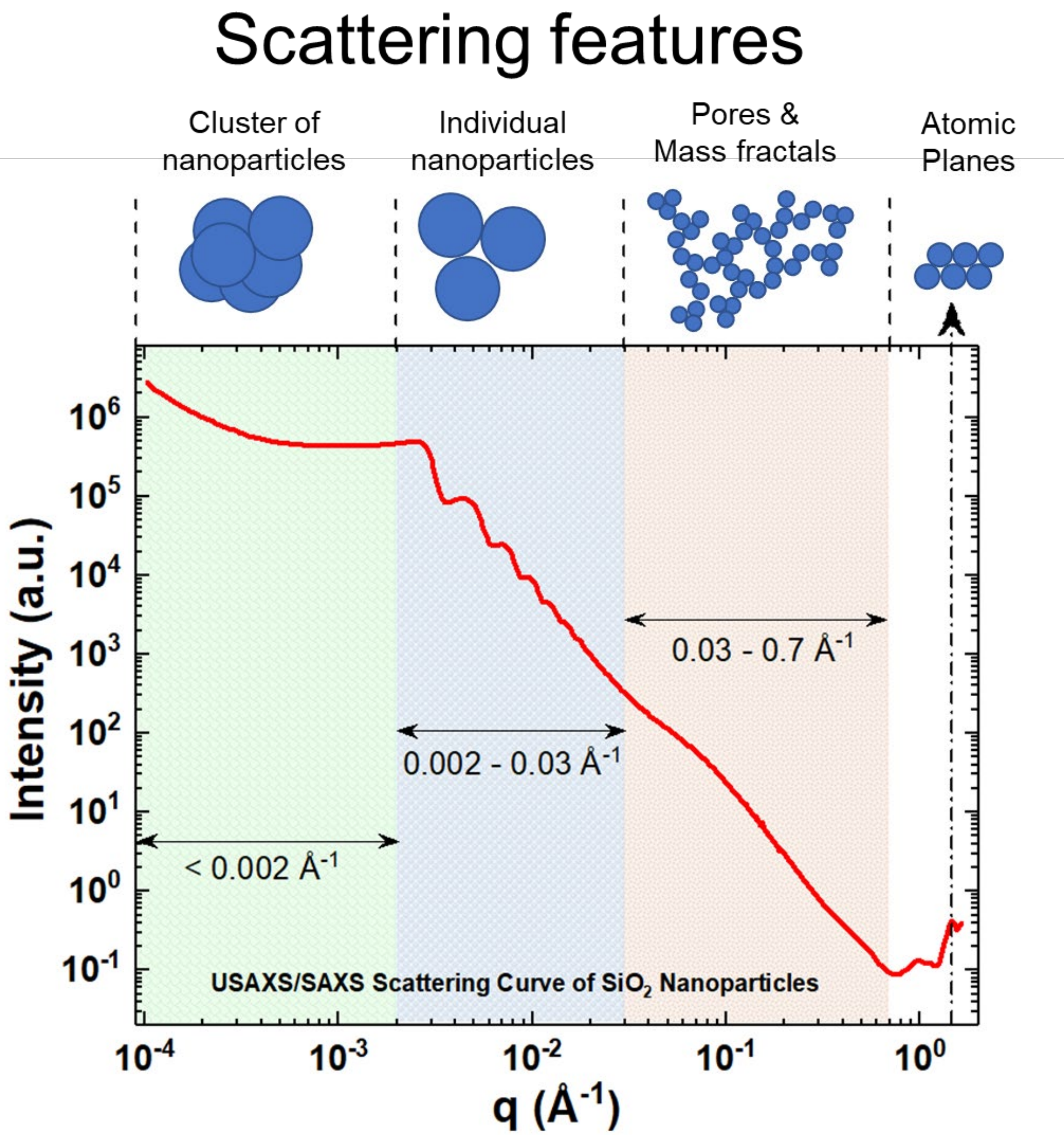

Figure 1. Representative ultra-small and small angle X-ray scattering (USAXS/SAXS) experimental curve of SiO_2 nanoparticles. The curve is divided into three different regions which were modeled to obtain the information about the physical features of interest.

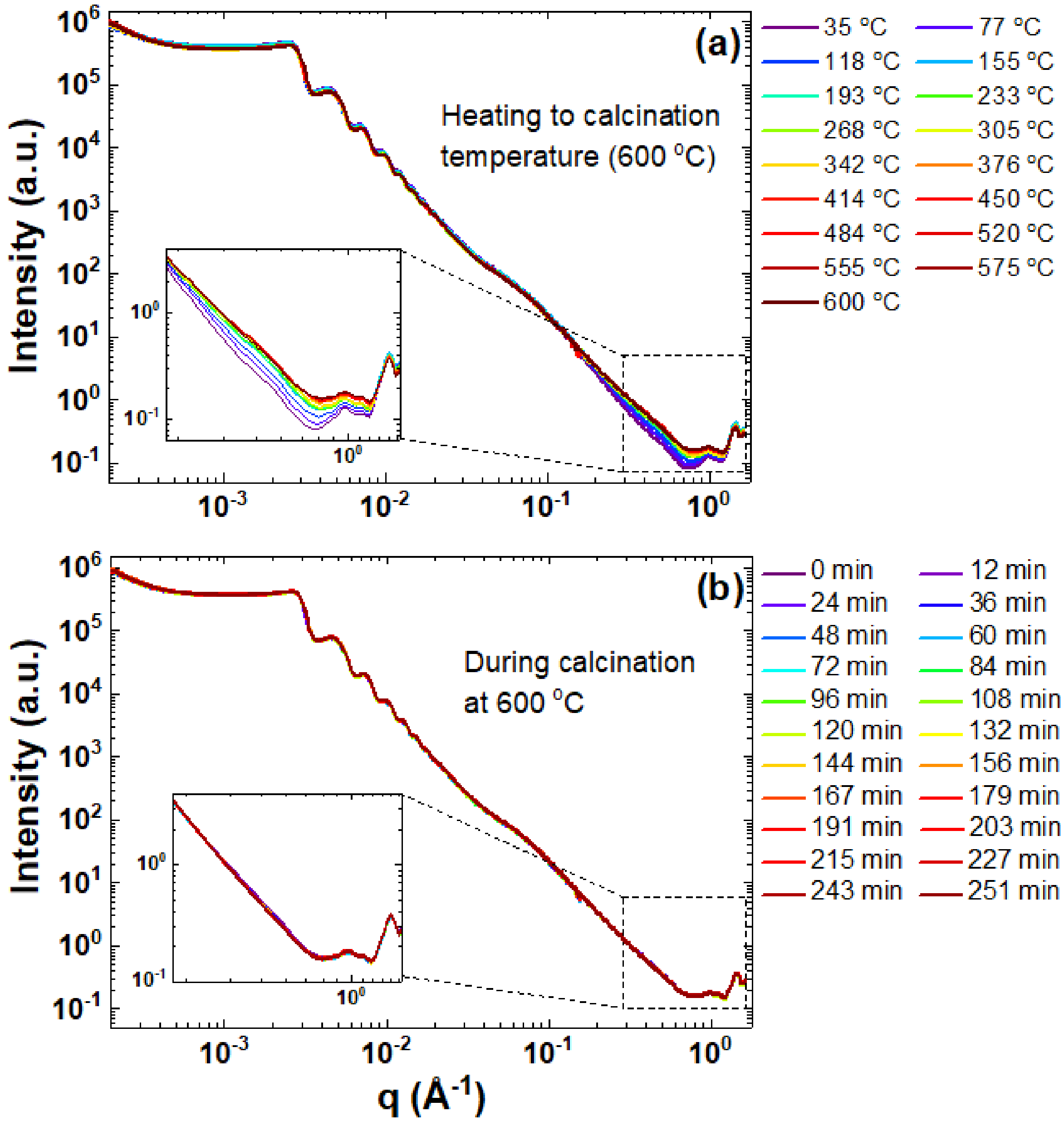

Figure 2. Ultra-small and small angle X-ray scattering (USAXS/SAXS) experimental data represent changes in the microstructural features of SiO_2 nanoparticles during heating to calcination temperature **(a)** and during calcination at 600 °C **(b)**.

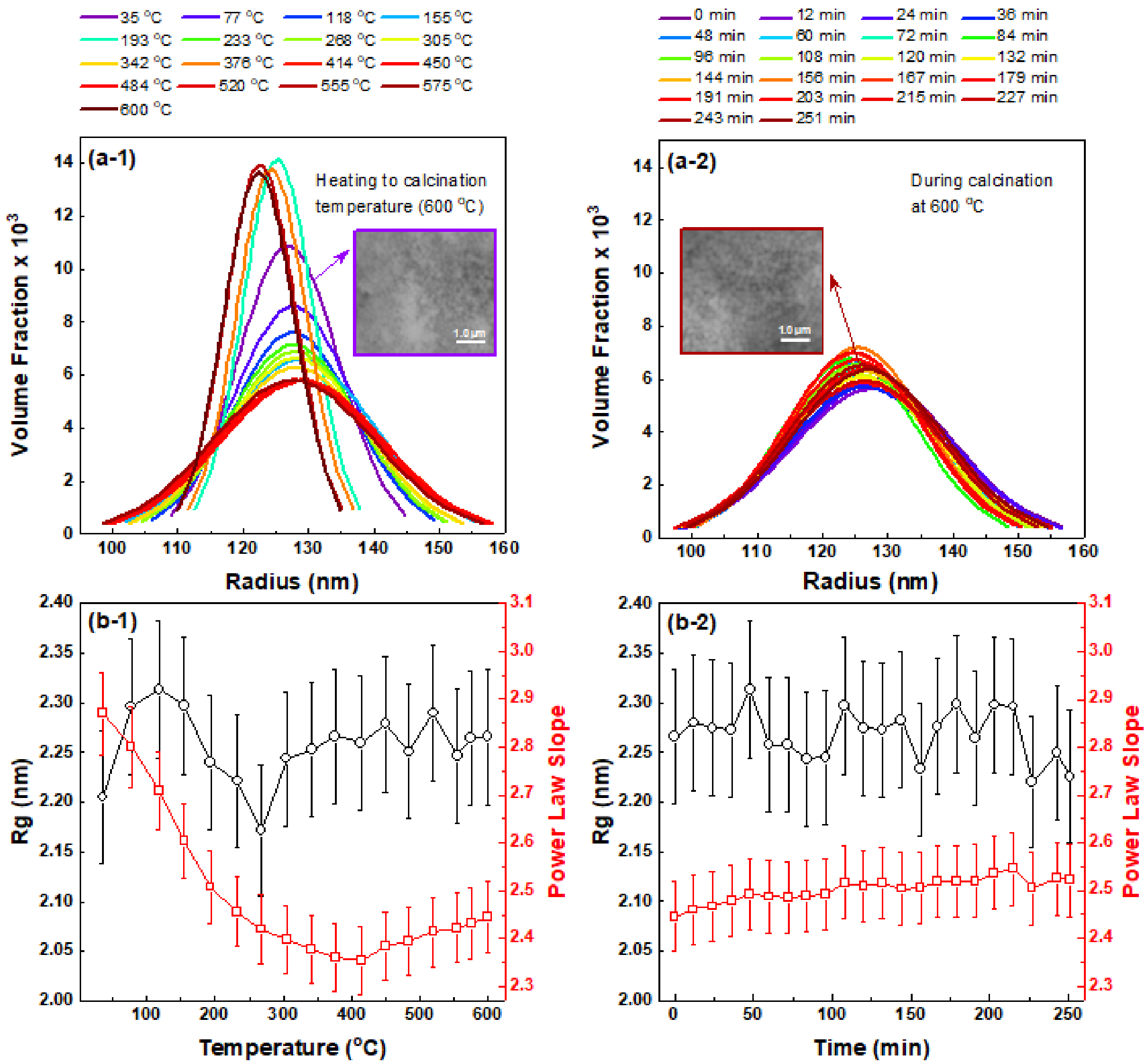

Figure 3. Particle size volume fraction distributions of silica nanoparticles approximated in the q-range of 0.002-0.03 Å^{-1} on heating to calcination temperature **(a-1)** and during the calcination process **(a-2)**. The changes in the pore morphology in the q-range of 0.03-0.7 Å^{-1} as represented by the characteristic radius of gyration (R_g) (black curve) and the power-law slope (red curve) during the temperature ramp to achieve the calcination temperature (**b-1**) and at the calcination temperature (**b-2**). The error bars on R_g values and power-law slopes correspond to 3% of error in calculated values. The insets in **(a-1)** and **(a-2)** represent the corresponding scanning electron micrographs.

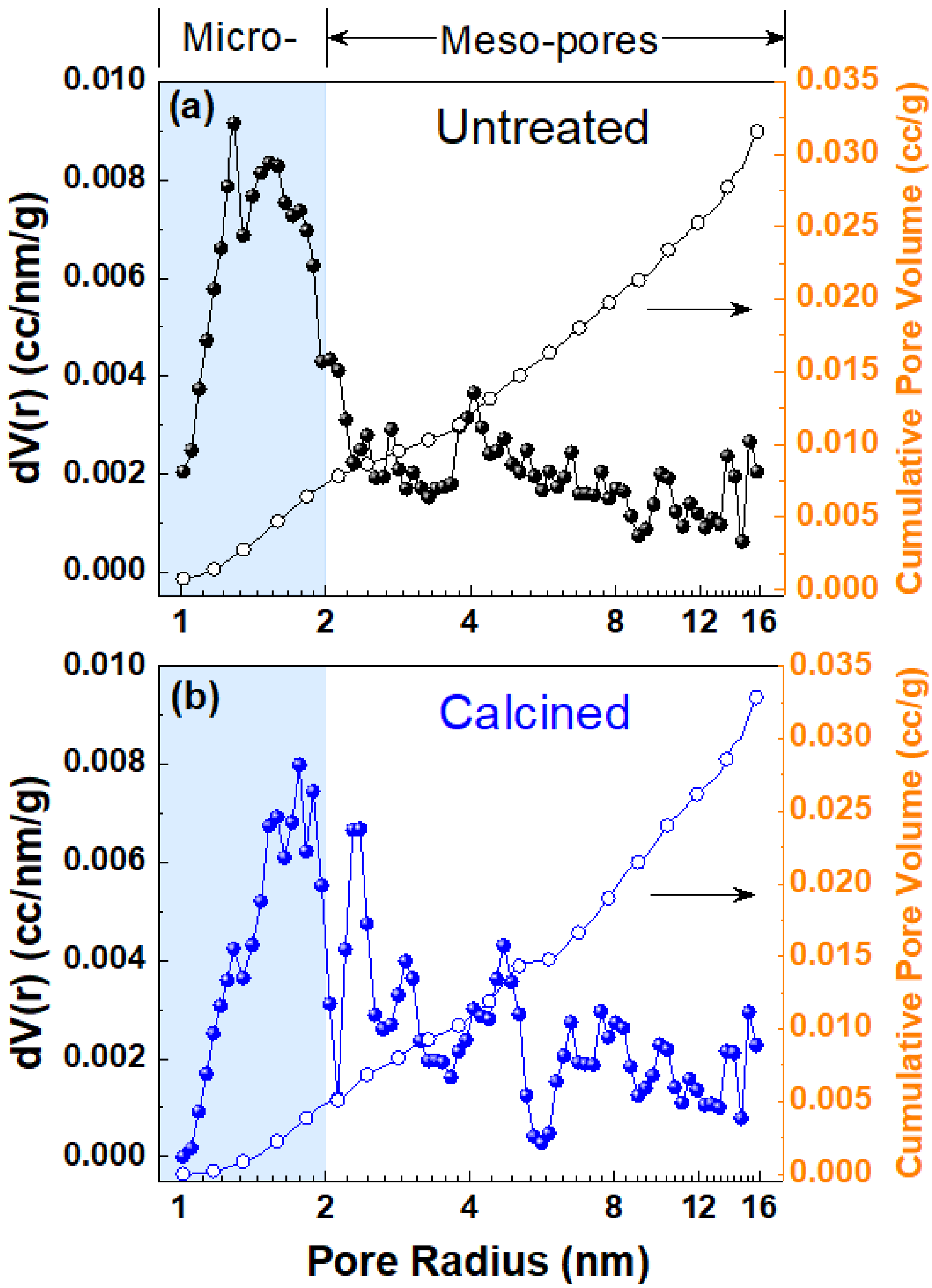

Figure 4. Pore size distributions and cumulative pore volumes of untreated **(a)**, and calcined **(b)** silica nanoparticles. SiO_2 nanoparticles were prepared by the modified Stöber method and calcined at 600 °C for 4 hours.

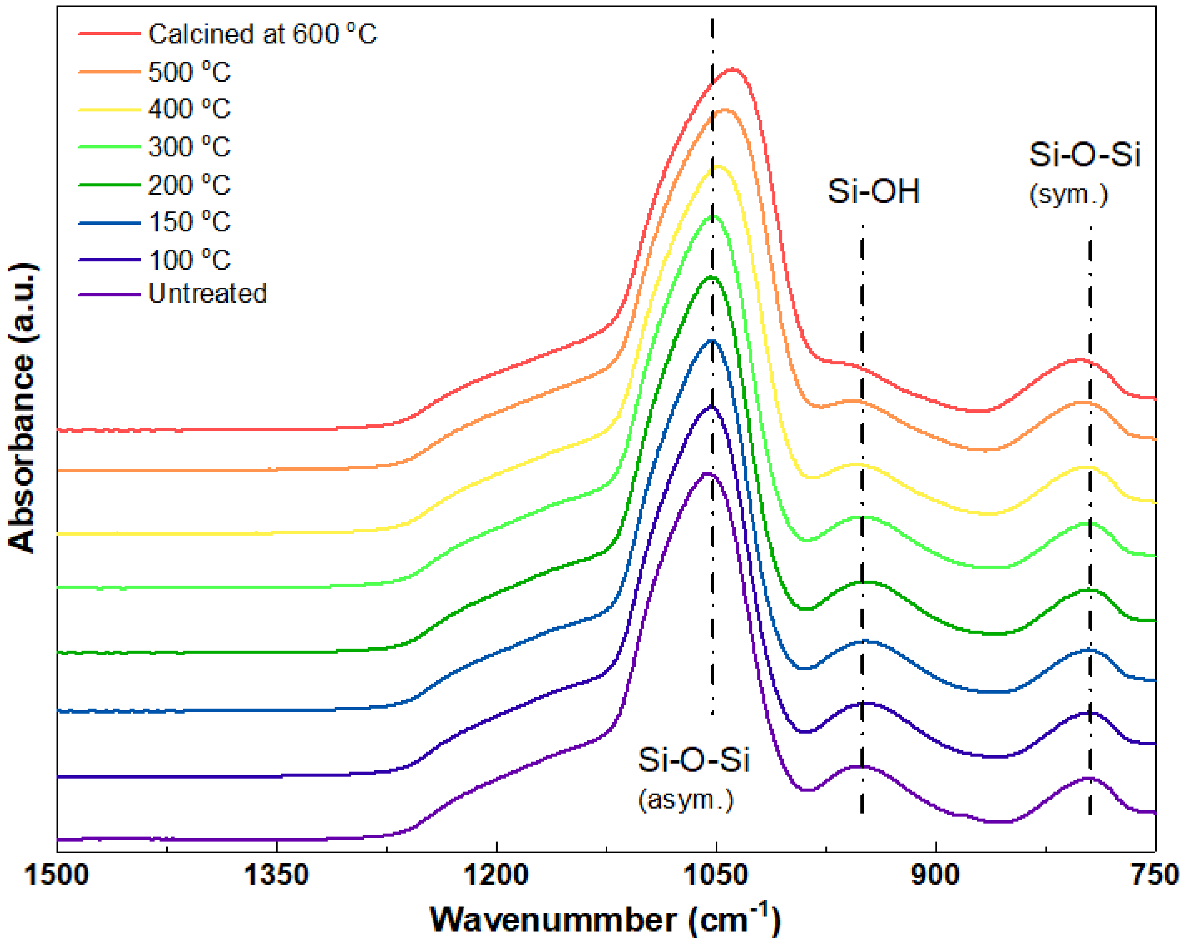

Figure 5. Changes in the Si-OH and Si-O-Si features for SiO_2 nanoparticles heated to different temperatures and calcined at 600 °C measured using Attenuated Total Reflectance Fourier Transform Infrared Spectroscopy (ATR-FTIR). Bands around 795 cm^{-1}, 950 cm^{-1}, and 1054 cm^{-1} correspond to Si-O-Si (sym.), Si-OH, and Si-O-Si (asym.) vibrations, respectively. With an increase in temperature, the Si-O-Si asymmetric band broadens while Si-OH vibration band ~950 cm^{-1} appears to be diminished in the calcined sample as a result of dehydroxylation of silica.

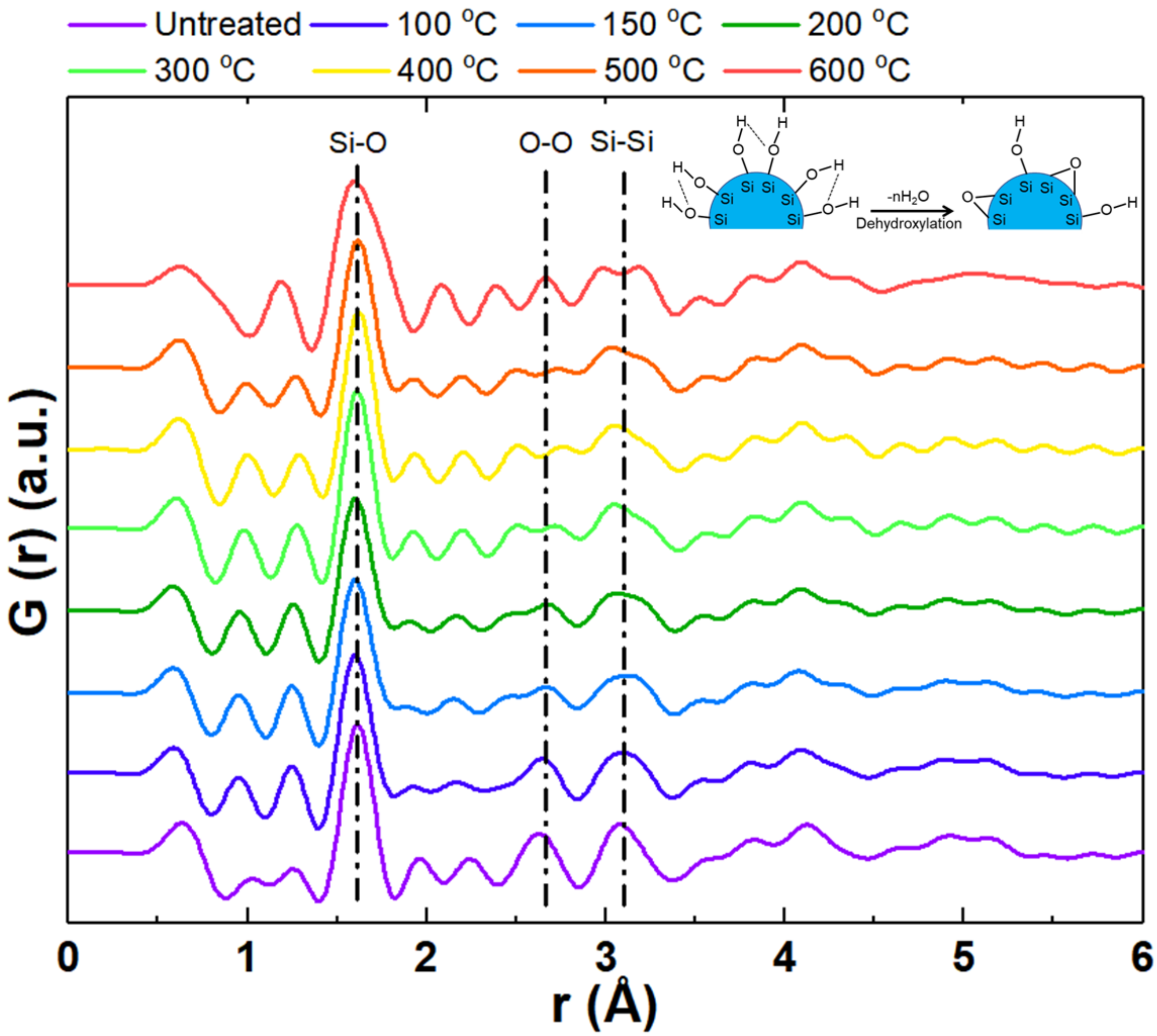

Figure 6. The pair distribution function (PDF) curves calculated from total X-ray scattering data during the in-operando heating of silica nanoparticles to calcination temperature (600 °C). Inset shows the schematic of dehydroxylation process i.e., breakage of silanol (Si-OH) bonds and formation of new siloxane (Si-O-Si) bridges.

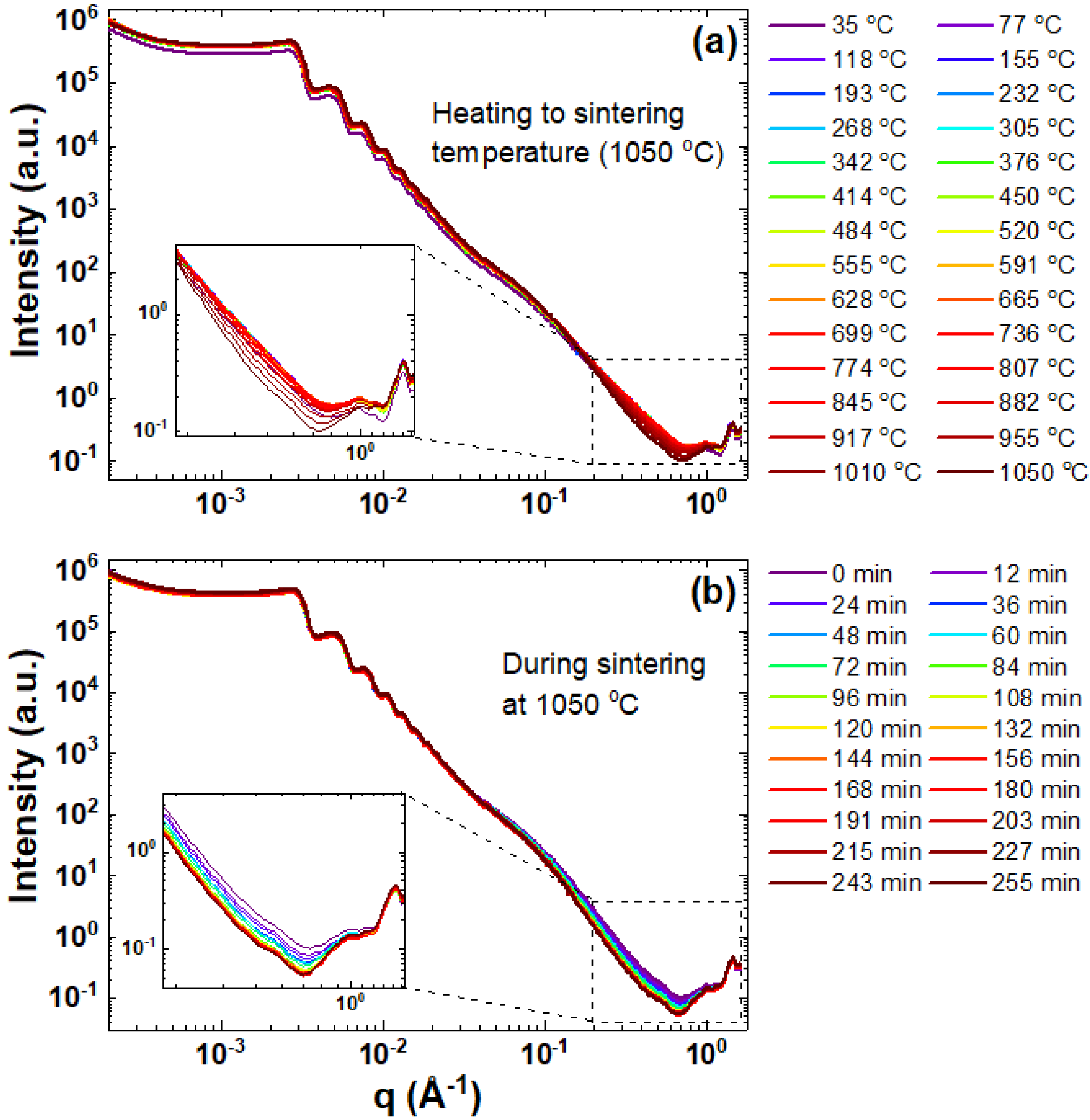

Figure 7. Ultra-small and small angle X-ray scattering (USAXS/SAXS) experimental data represent changes in the microstructural features of calcined SiO_2 nanoparticles during heating to sintering temperature **(a)** and during sintering at 1050 °C **(b)**.

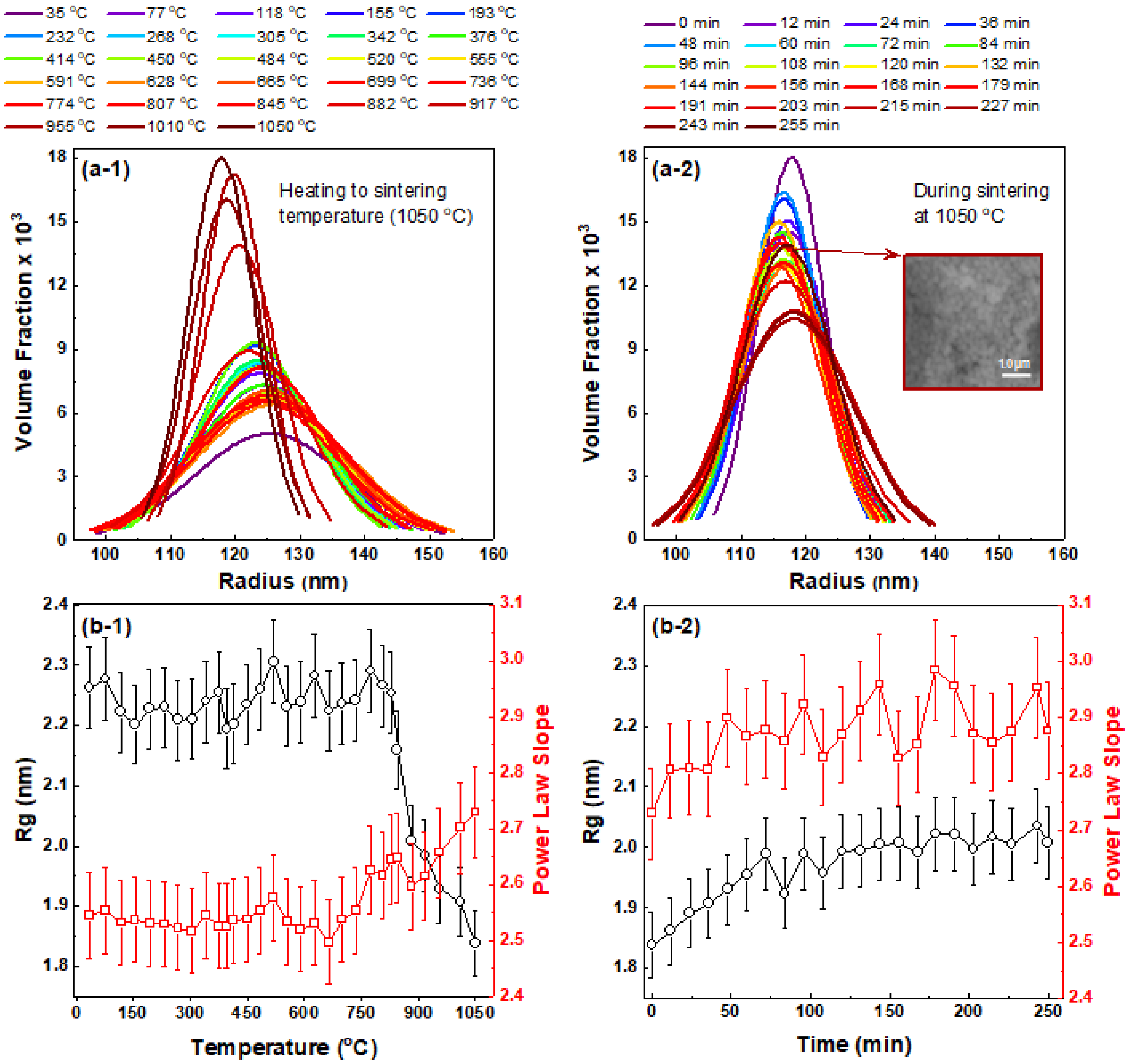

Figure 8. Particle size volume fraction distributions of calcined silica nanoparticles on heating to the sintering temperature **(a-1)** and during the sintering process **(a-2)** approximated in the q-range of 0.002-0.03 Å^{-1}. The changes in the pore morphology in the q-range of 0.03-0.7 A^{-1} as represented by the characteristic radius of gyration (R_g) (black curve) and the power-law slope (red curve) during the temperature ramp to achieve sintering temperature (**b-1**) and at the sintering temperature (**b-2**). The error bars on R_g and power-law values correspond to 3% of error in calculated values. The inset in **(a-2)** represent the corresponding scanning electron micrograph.

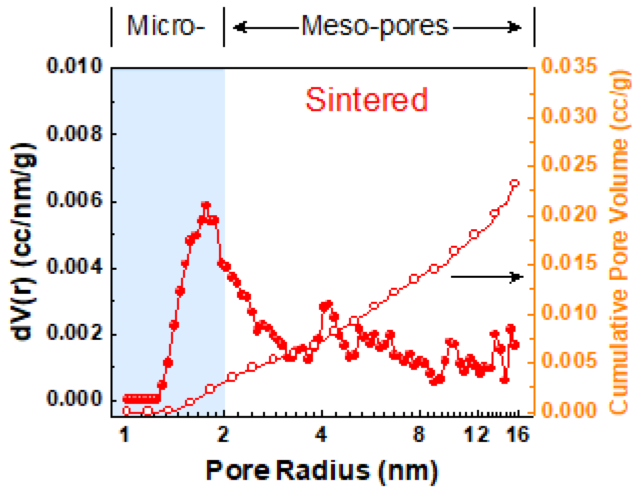

Figure 9. Pore size distribution and cumulative pore volume of sintered SiO_2 nanoparticles. SiO_2 nanoparticles were prepared by modified Stöber method, calcined at 600 °C for 4 hours and sintered at 1050 °C for 4 hours.

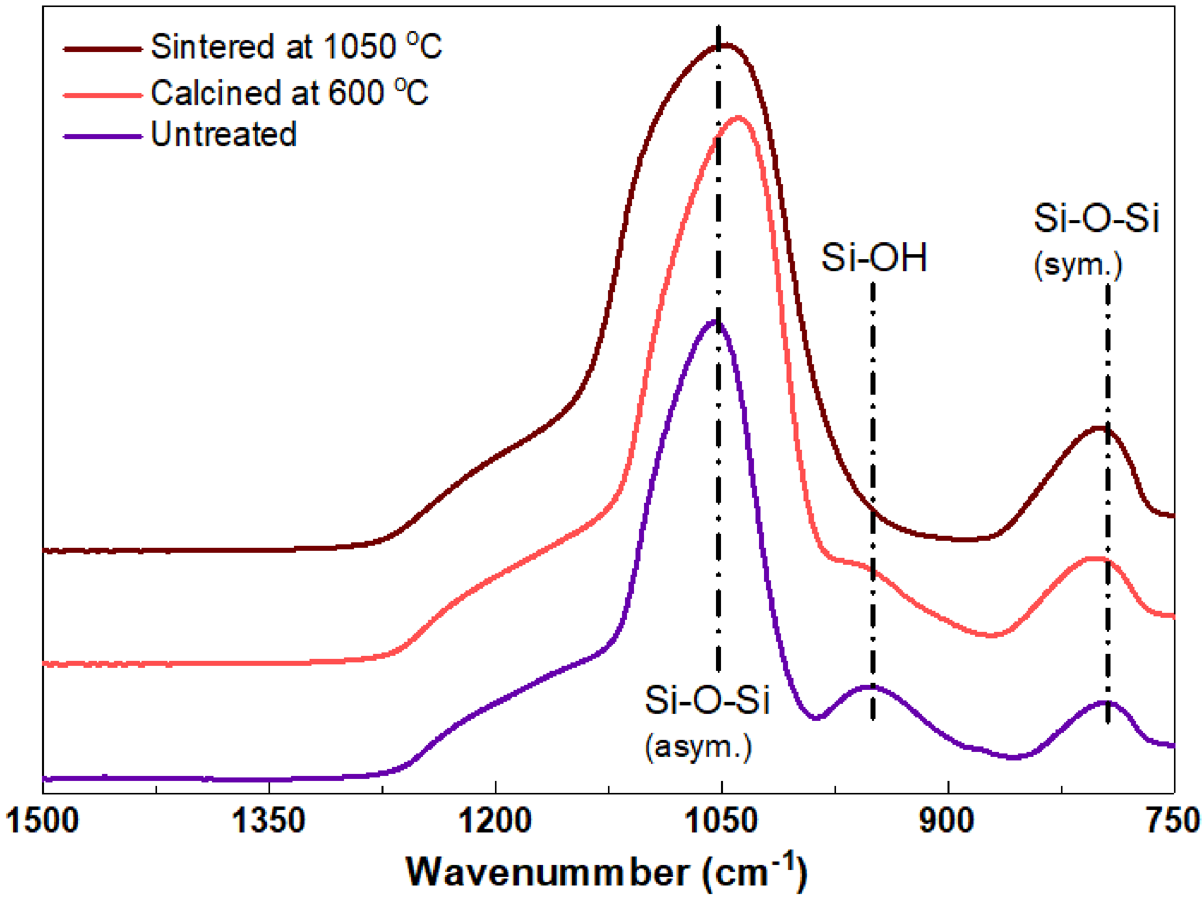

Figure 10. Comparison of changes in the Si-OH and Si-O-Si features for untreated, calcined and sintered SiO_2 nanoparticles measured using Attenuated Total Reflectance Fourier Transform Infrared Spectroscopy (ATR-FTIR). Bands around 795 cm^{-1}, 950 cm^{-1}, and 1054 cm^{-1} correspond to Si-O-Si (sym.), Si-OH, and Si-O-Si (asym.) vibrations, respectively. With an increase in temperature, the Si-O-Si asymmetric band broadens while Si-OH vibration band ~950 cm^{-1} diminishes completely as a result of sintering at 1050 °C.

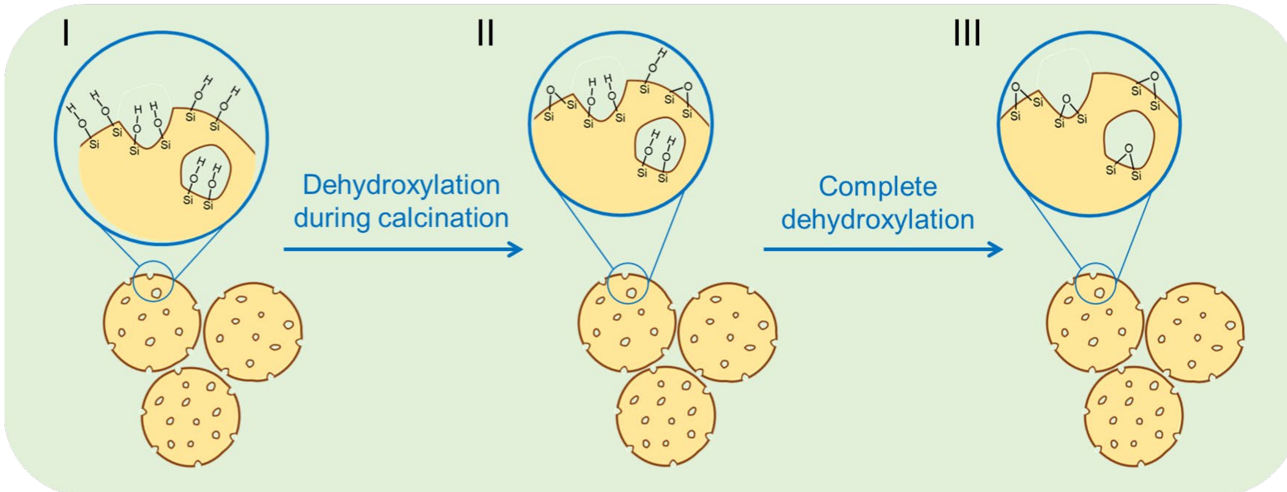

Figure 11. Schematic representation of chemo-morphological changes that occurring during sintering of silica nanoparticles. As a result of heating to calcination temperature (600 °C), primary dehydroxylation of -OH groups from silanol (Si-OH) bonds generate siloxane (Si-O-Si) bridges (change from **I** to **II**). Heating the calcined nanoparticles to sintering temperature (1050 °C) results in secondary dehydroxylation, which starts after 800 °C where Si-O-Si bridges could form inside the pores (**III**).

Graphical Abstract